JGR Atmospheres

Key Points:

- Satellite-retrieved carbon monoxide (CO) plumes from the Australian fires circumvent the Southern Hemisphere
- Satellite-retrieved methanol (CH_3OH) shows downwind enhancement of CH_3OH:CO ratio suggesting in-plume secondary CH_3OH production as well as direct emission
- Substantial enhancements in methane (CH_4) are detected from space

Supporting Information:

Supporting Information may be found in the online version of this article.

Correspondence to:

R. J. Pope,
earrjpo@leeds.ac.uk

Large Enhancements in Southern Hemisphere Satellite-Observed Trace Gases Due to the 2019/2020 Australian Wildfires

Richard J. Pope[1,2] , **Brian J. Kerridge[3,4]**, **Richard Siddans[3,4]**, **Barry G. Latter[3,4]** , **Martyn P. Chipperfield[1,2]** , **Stephen R. Arnold[1]** , **Lucy J. Ventress[3,4]**, **Matilda A. Pimlott[1]**, **Ailish M. Graham[1]**, **Diane S. Knappett[3,4]**, and **Richard Rigby[1,5]**

[1]School of Earth and Environment, University of Leeds, Leeds, UK, [2]National Centre for Earth Observation, University of Leeds, Leeds, UK, [3]Remote Sensing Group, STFC Rutherford Appleton Laboratory, Chilton, UK, [4]National Centre for Earth Observation, STFC Rutherford Appleton Laboratory, Chilton, UK, [5]Centre for Environmental Modelling and Computation, University of Leeds, Leeds, UK

Abstract The 2019/2020 Australian wildfires emitted large quantities of atmospheric pollutant gases and aerosols. Using state-of-the-art near-real-time satellite measurements of tropospheric composition, we present an analysis of several emitted trace gases and their long-range transport, and compare to the previous (2018/2019) fire season. Observations of carbon monoxide (CO) show that fire emissions were so intense that the distinct Australian fire plume managed to circumnavigate the Southern Hemisphere (SH) within a few weeks, with eastward propagation over the South Pacific, South America, the South Atlantic, Africa, and the Indian Ocean. Elevated atmospheric methane levels were also detected in January 2020 fire plumes over the Pacific, defined using CO as a plume tracer, even though sampling was restricted spatially by aerosols and clouds. Observations also show significant enhancements of methanol (CH_3OH) from the fires, where CH_3OH:CO enhancement ratios increased within the aged plume downwind over the South Pacific indicating secondary in-plume CH_3OH formation.

Plain Language Summary The 2019/2020 Australian wildfires emitted large quantities of smoke and gaseous pollutants. Using satellite observations, we analyze the long-range transport of several trace gases and compare with the previous (2018/2019) fire season. The 2019/20 fires were so intense that a distinct plume of carbon monoxide was observed to propagate around the entire Southern Hemisphere in just a few weeks. Enhancement of methane was also detected in the plume along with substantial quantities of methanol. The ratio between methanol and carbon monoxide increased over the Southern Pacific suggesting the secondary formation of methanol within the fire plume as it propagated eastwards.

1. Introduction

Vegetation fires occur regularly in Australia between the months of August and December (Giglio et al., 2013; van der Werf et al., 2017). Burning activity predominantly occurs in northern Australia, but is widespread across the continent (Andela et al., 2017). Giglio et al. (2013) suggested that the majority of vegetation fires take place on savanna and shrubland, but in south-eastern Australia forest fires are most prevalent (Bradstock et al., 2012; van der Werf et al., 2010). Over recent decades, there have been large-scale decreases in Australian fire activity (Andela et al., 2017; Rabin et al., 2015). However, with present and future climate and land-use change, conditions in Australia are predicted to yield more frequent large-scale fire events (Clarke et al., 2011; Di Virgilio et al., 2019; Pitman et al., 2007). According to the Australian Bureau of Meteorology (2020), the 2019 summer was the warmest (1.52°C above the national average, 1961–1990) and driest (rainfall 40% lower than average) season on record. This provided suitable conditions for wildfires to ignite and spread.

The Australian wildfires of the 2019/2020 fire season, colloquially known as the "black summer," represented some of the largest events in recent decades. The fires burned over 110,000 km^2 of bush, forest and parks (BBC, 2020). The majority of the fire activity occurred in south-eastern Australia (New South Wales and Victoria), which is predominantly eucalyptus forest and woodland (SOTE, 2016). The fires caused 33 deaths (BBC, 2020) and killed over approximately 1 billion animals (UoS, 2020). In comparison, the Black

Saturday fires (February 2009) in Victoria burned approximately 4,500 km^2 and killed 173 people (Siddaway & Petelina, 2011). Though the 2019/2020 fire death toll was lower, the burned area (BA) was much larger producing substantial quantities of smoke and pollutants.

Vegetation fires emit large quantities of smoke/aerosols and trace gases, which have important impacts on climate and the atmospheric radiation balance (Li et al., 2017; Rowlinson et al., 2019) and surface air quality (AQ, Bowman & Johnston, 2005; Haikerwal et al., 2016; Kiely et al., 2019; Reisen et al., 2005). The 2019/2020 Australian fires emitted approximately 250 million tonnes of carbon dioxide (CO_2), equivalent to nearly half the country's annual anthropogenic emissions (Hope, 2020). This combination of fuel type, fire intensity and coverage, yielded large-scale fire plumes causing intense local pollution as well as long-range pollution transport. Wildfire-driven pyro-convection propagated vertically up into the stratosphere, reaching approximately 30 km (Kablick et al., 2020; Khaykin et al., 2020; Ohneiser et al., 2020; Schwartz et al., 2020) over the South Pacific. In comparison, the Black Saturday fire plume reached 22 km (Siddaway & Petelina, 2011).

In this study, we use state-of-the-art satellite retrievals to provide detailed analysis of the spatial and temporal evolution of several trace gas distributions sourced from the 2019/2020 Australian fires. While available for the stratosphere, such capabilities were in their infancy when previous major burning events occurred in Australia (e.g., February 2009).

2. Observations

2.1. Fire Data Sets

We use two different satellite-derived fire activity datasets: fire radiative power (FRP) from the Global Fire Assimilation System (GFAS vn1.2; Kaiser et al., 2012) and BA from the Fire INventory from NCAR (FINN near-real-time (NRT) vn1.0; Wiedinmyer et al., 2011). Both products are provided at a daily temporal resolution and are based on direct Moderate Resolution Imaging Spectroradiometer (MODIS) measurements (e.g., FRP and thermal anomalies). These quantities are merged with secondary information (including land surface type and emission factors) to derive top-down emissions for trace gases and aerosols (Kiely et al., 2019; Wooster et al., 2018).

2.2. Trace Gas Data Sets

In this study we use trace gas retrievals from the Infrared Atmospheric Sounding Interferometer (IASI). IASI is a Michelson interferometer which observes the spectral range 645–2,760 cm^{-1} with spectral sampling of 0.25 cm^{-1} (Illingworth et al., 2011). It measures simultaneously in four fields of view (FOV, each circular at nadir with a diameter of 12 km) which are scanned across track to sample a 2,200 km-wide swath (Clerbaux et al., 2009). IASI is one of a suite of nadir-sounders flying on Eumetsat's MetOp-A, -B and -C satellites in sun-synchronous polar orbits with local overpass times of 9.30 (day) and 21.30 (night). Here we use carbon monoxide (CO), methanol (CH_3OH), and methane (CH_4) data from MetOp-B produced by NRT processing systems developed by the Rutherford Appleton Laboratory (RAL). CO profiles are co-retrieved with column amounts of CH_3OH, other trace gases and dust in an extended version of RAL's Infrared-Microwave-Sounding (IMS) scheme, which is described in the Supporting Information Text S1. IMS was developed originally to retrieve temperature, water vapor, ozone, surface spectral emissivity and cloud jointly from co-located measurements by IASI, the Microwave Humidity Sounder (MHS) and the Advanced Microwave Sounding Unit (AMSU-A) on MetOp-A (RAL Space, 2015). CH_4 data are retrieved by an improved version of the IASI scheme reported by RAL Space (2015), which is detailed by Siddans et al. (2017). Data are available from the Centre of Environmental Data Analysis (CEDA, Siddans et al., 2020). CO and CH_3OH have been quality filtered for a geometric cloud fraction of 0.5 or less (0.1 or less for CH_4 given the greater sensitivity to interference from cloud/aerosol) and a cost value of 1,000.0 or less (120 or less for CH_4 plus a convergence flag equally 1.0). For CO and CH_3OH, we experimented with a stricter geometric cloud fraction threshold of <0.2. We found this had negligible impact on the scientific results, but did reduce the spatial coverage, making the fire signals noisier. Hence we used the <0.5 cloud fraction threshold. We have also investigated more localized responses in the short-lived nitrogen dioxide (NO_2) utilizing tropospheric column NO_2 ($TCNO_2$) data from the TROPOspheric Monitoring Instrument (TROPOMI) on-board the ESA's Sentinel-5 Precursor
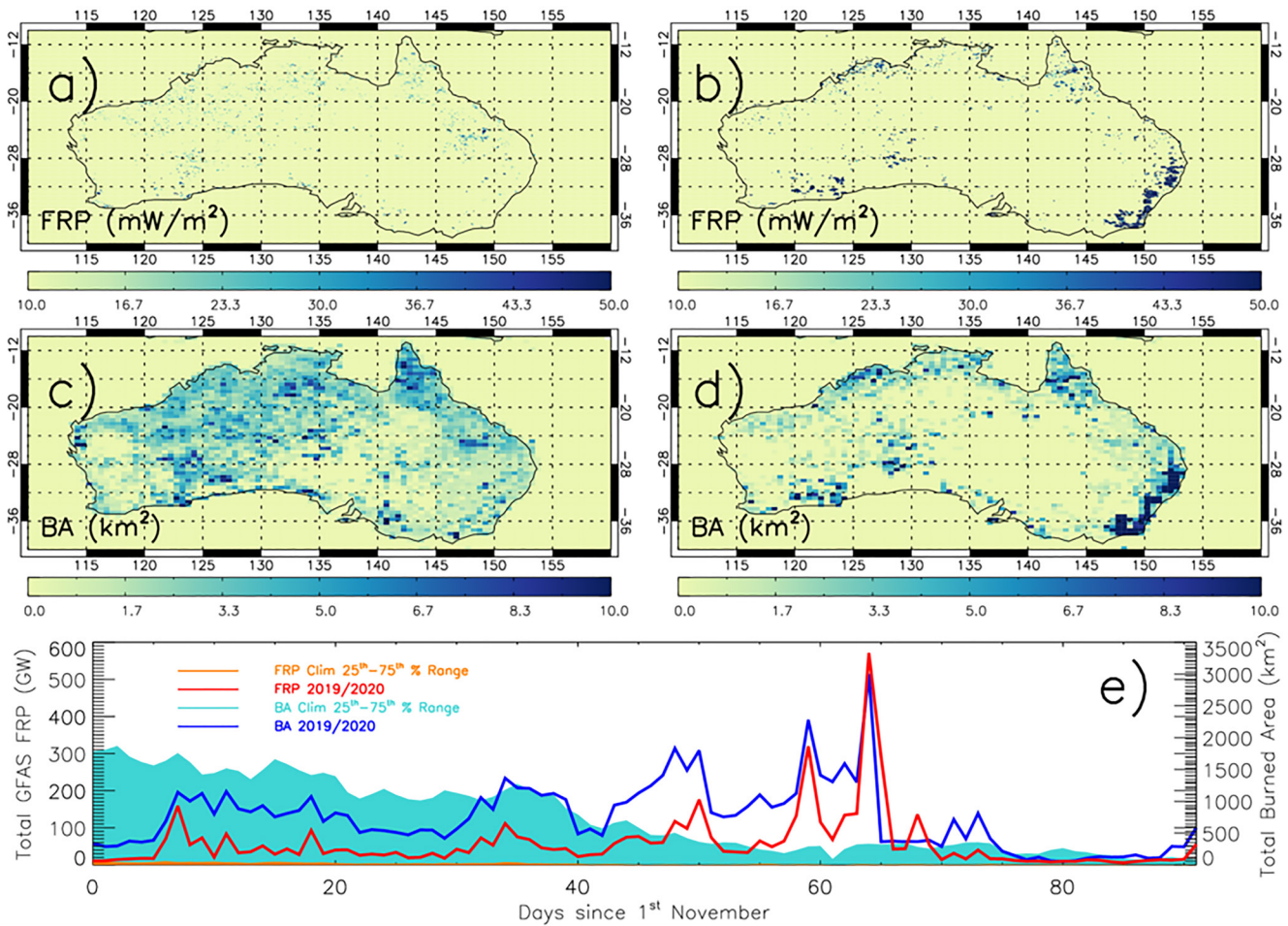
Figure 1. Global Fire Assimilation System (GFAS) fire radiative power (FRP, mW/m^2) for (a) November-December-January (NDJ) climatology (2009–2019) and (b) NDJ 2019/2020. Panels (c) and (d) show Fire INventory from NCAR (FINN) burned area (BA, km^2) for (c) NDJ climatology (2009–2019) and (d) NDJ 2019/2020. Panel (e) shows daily time series of accumulated FRP (GW, blue solid line) and BA (km^2, red solid line) across Australian for NDJ 2019/2020. The orange and light blue shading represent the 25–75th percentiles spread in the climatology for FRP and BA, respectively.

(S5P) satellite (Veefkind et al., 2012). S5P was launched in October 2017 into a sun-synchronous polar orbit with a local overpass time of approximately 13.30. TROPOMI is a nadir-viewing instrument with spectral ranges of 270–500 nm (UV-Vis), 675–775 nm (near-infrared, NIR), and 2305–2385 nm (shortwave-infrared, SWIR). The TROPOMI retrievals represent the highest resolution of any current tropospheric trace gas sensor with a nadir horizontal resolution of 3.5×7.0 km in the UV-Vis-NIR and 7.0×7.0 km in the SWIR. The data were filtered for a radiance cloud fraction of <0.5 and a quality flag >0.75.

3. Results

3.1. Fire Activity

During the 2019/2020 fire season (November-December-January, NDJ), satellite observations detected substantially larger fire activity on the Australian south-eastern coastline around highly populated regions such as Sydney compared to the average of the previous 10 seasons (NDJ 2009–2019 climatology). GFAS FRP suggests that on average (NDJ climatology) (Figure 1a) there was limited fire activity over south-eastern Australia (i.e., 10–20 mW/m^2). The peak activity was more widespread across the north-western territories with FRP typically between 20 and 30 mW/m^2. However, in NDJ 2019/2020 the entire Australian south-eastern coastline experienced large-scale fires with intensities well above 50 mW/m^2 (Figure 1b). This is supported by the FINN BA (Figures 1c and 1d) with fire events peaking above 10 km^2 widespread
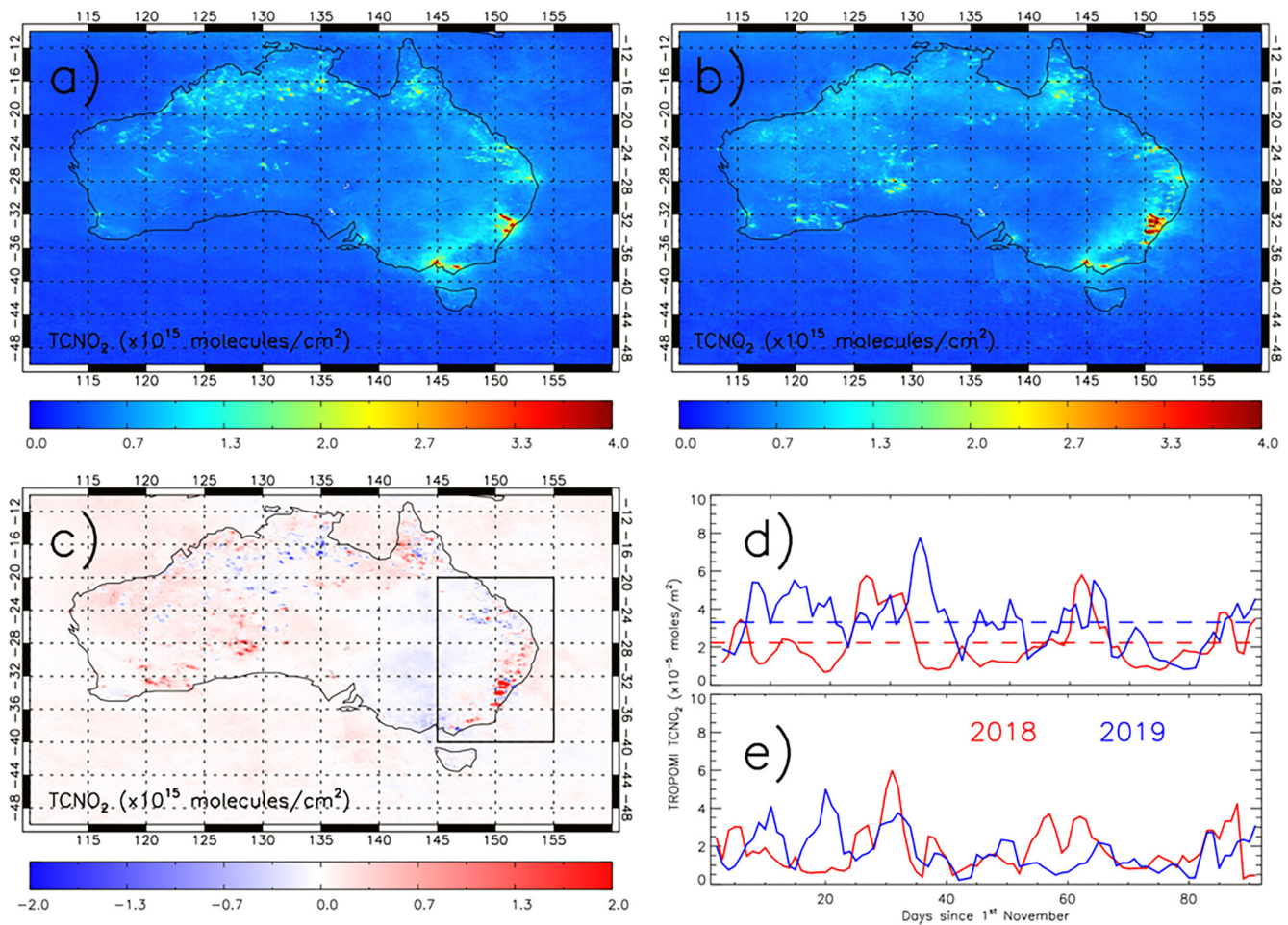
Figure 2. TROPOspheric Monitoring Instrument (TROPOMI) tropospheric column NO_2 ($TCNO_2$, 10^{15} molecules/cm²) for (a) December 2018, (b) December 2019, and (c) difference December 2019–2018. The black box in panel (c) represents the region used in panels (d) and (e). Panel (d) shows time series of regional November-December-January (NDJ) $TCNO_2$ for 2018/2019 (red) and 2019/2020 (blue) weighted by regional fire radiative power (FRP). Dashed lines represent the 3-months average. Panel (e) represents regional 2018/2019 and 2019/2020 $TCNO_2$ weighted by 2019/2020 and 2018/2019 FRP, respectively.

across the south-east coast. In contrast, the fire events in the NDJ climatology predominantly occurred over the north-western territories and northern coastlines, with lower BA between 3.0 and 7.0 km². Figure 1e shows the time-series of the total daily Australian FRP and BA for the climatological (median daily totals, 2009–2019) and 2019/2020 fire seasons. Between November 1, and January 31, the climatological FRP has a small range (i.e., 25th–75th percentiles) between approximately 0 and 10 GW. Climatological BA ranges between approximately near-zero and 1,700 km². However, the 2019/2020 FRP (BA) is typically between 20 (100) and 150 (1,700) GW (km²), but with peaks in late December (FRP = ~320 GW, BA = ~2,200 km²) and early January (FRP = ~580 GW, BA = ~3,000 km²). The peak FRP and BA values sit well outside the variability of the climatologies, highlighting the extreme fire activity experienced in the 2019/2020 fire season.

3.2. Nitrogen Dioxide

The response of $TCNO_2$ to the NDJ 2019/2020 Australian fires is less pronounced relative to the other trace gases investigated here due to the relatively short NO_2 lifetime of a few hours (Alvarado et al., 2010; Logan, 1983). In December 2018 (Figure 2a), there are clear $TCNO_2$ hotspots (0.5–1.5 × 10^{15} molecules/cm²) in the north-western territories which clearly overlap with GFAS FRP (Figure 1a). Similar relationships are seen near the coast in Queensland. Clear urban signals exist such as Sydney (over 4.0 × 10^{15} molecules/cm²), Melbourne (over 4.0 × 10^{15} molecules/cm²), and Brisbane/Adelaide (1.0–2.0 × 10^{15} molecules/cm²). However, in December 2019 (Figure 2b), there was a large spatial increase in $TCNO_2$ values

$> 4.0 \times 10^{15}$ molecules/cm^2 around Sydney. Again, these TCNO$_2$ hotspots are spatially correlated with fire activity (Figure 1) suggesting that fires have degraded the air quality in urban regions. Figure 2c shows the difference between December 2019 and 2018, where there are mixed TCNO$_2$ differences across the northern states, with enhancements ($0.0–1.0 \times 10^{15}$ molecules/cm^2) in the Western Australia territory and along the south-eastern coastline (2.0×10^{15} molecules/cm^2). To rule out other sources (e.g., urban) driving the TCNO$_2$ enhancement along the south-eastern coastline, TCNO$_2$ values have been weighted by FRP over the region (black box, Figure 2c) for the 2018/2019 (Figure 2d, red line) and 2019/2020 (Figure 2d, blue line) seasons. The FRP-weighted TCNO$_2$ signal for both seasons highlights sizable variability, but 2019/2020 TCNO$_2$ values are larger in the first 20 days of November ($3.0–6.0 \times 10^{15}$ molecules/cm^2), peak in early December ($>7.5 \times 10^{15}$ molecules/cm^2) and remain larger for most of December. Overall, the time period average 2018/2019 and 2019/2020 FRP-weighted TCNO$_2$ values are approximately 2.2×10^{15} molecules/cm^2 and 3.3×10^{15} molecules/cm^2, respectively. To reduce the likelihood of this fire-TCNO$_2$ signal being dominated by other sources, Figure 2e shows time-series where the 2019/2020 TCNO$_2$ has been weighted by the 2018/2019 FRP and the 2018/2019 TCNO$_2$ has been weighted by the 2019/2020 FRP. The 2018/2019 TCNO$_2$ time-series (red lines in Figures 2d and 2e) are generally similar suggesting the NO$_2$ signal is not overly dependent on fire activity. However, in the 2019/2020 season (blue lines in Figures 2e and 2d), the time-series are substantially different where the 2019/2020 TCNO$_2$ series weighted by the 2018/2019 FRP is lower ($0–3 \times 10^{15}$ molecules/cm^2). Therefore, the large 2019/2020 TCNO$_2$ values are highly likely to be driven primarily by fire activity along the south-east coastline, especially around Sydney.

3.3. Carbon Monoxide

The 2019/2020 Australian fire season produced extensive quantities of emitted CO, as observed by IASI. Figure 3c shows a large total-column CO (TCCO) plume originating over south-eastern Australia and propagating across the entire Pacific, reaching South America. Here, the TCCO ranges between approximately $16–21 \times 10^{17}$ molecules/cm^2, peaking over the Australian coastline and midway between continents in the NDJ period 2019/2020. In the previous burning season (NDJ 2018/2019), TCCO was considerably lower and ranged between $10–13 \times 10^{17}$ molecules/cm^2, with no obvious fire signal over Australia (Figure 3a). Figure 3e shows the difference between fire seasons to be widespread and large ($1.5–7.5 \times 10^{17}$ molecules/cm^2) across the Pacific. Peak inter-year differences of over 5.0×10^{17} molecules/cm^2 occur over south-eastern Australia and the mid-Pacific, as the plume propagates eastwards. The inter-year differences are significant over large areas (99% confidence level based on the Student t-test and where absolute mean differences are greater than 1.0×10^{17} molecules/cm^2) as shown by the green polygon-outlined regions.

During the 2018/2019 season, fire plumes of limited extent were detected, with moderate CO outflow from the east coast in November 2018 peaking at approximately 19.0×10^{17} molecules/cm^2 (Figure 3b). In NDJ 2019/2020, there is large and frequent CO outflow throughout the entire season (Figure 3d). TCCO peaks at more than 30.0×10^{17} molecules/cm^2 and persists across the $20°–40°$S band. Figure 3f shows that the inter-year difference exceeds 15.0×10^{17} molecules/cm^2 and the larger quantities of CO propagating out into the Pacific (Figure 3c). CO outflow from the peak fire activity (Figure 1e) in late December 2019/early January 2020 went on to circumnavigate the entire SH (Figure 4). Between December 27, 2019 and January 9, 2020, the fire emissions led to large quantities of CO ($>25 \times 10^{17}$ molecules/cm^2), which formed large-scale plumes propagating toward South America. Pyroconvection during this period uplifted plumes to altitudes where CO and other trace gases could more easily be detected by IASI (i.e., colder temperatures and above clouds). In the following fortnight, January 10–23, 2020, these plumes reached South America (peak TCCO $> 20.0 \times 10^{17}$ molecules/cm^2) and started propagating into the South Atlantic ($15–18 \times 10^{17}$ molecules/cm^2). A week later, the TCCO plume reached southern Africa (no local fire sources apparent there, unlike e.g., November 15–28, 2019) with values still between 15 and 18×10^{17} molecules/cm^2. The TCCO quantities were also enhanced to $14–16 \times 10^{17}$ molecules/cm^2 over the Indian Ocean, reaching the Australian west coastline and fully encircling the SH. Over south-eastern Australia (black box in Figure 2c), the 2019/2020 fires (NDJ) emitted 9.06 Tg of CO (1.73 times larger than the 2018/2019 annual total anthropogenic Australian CO emissions; NPI, 2020) in comparison to 0.33 Tg in NDJ 2018/2019, based on FINN emissions.
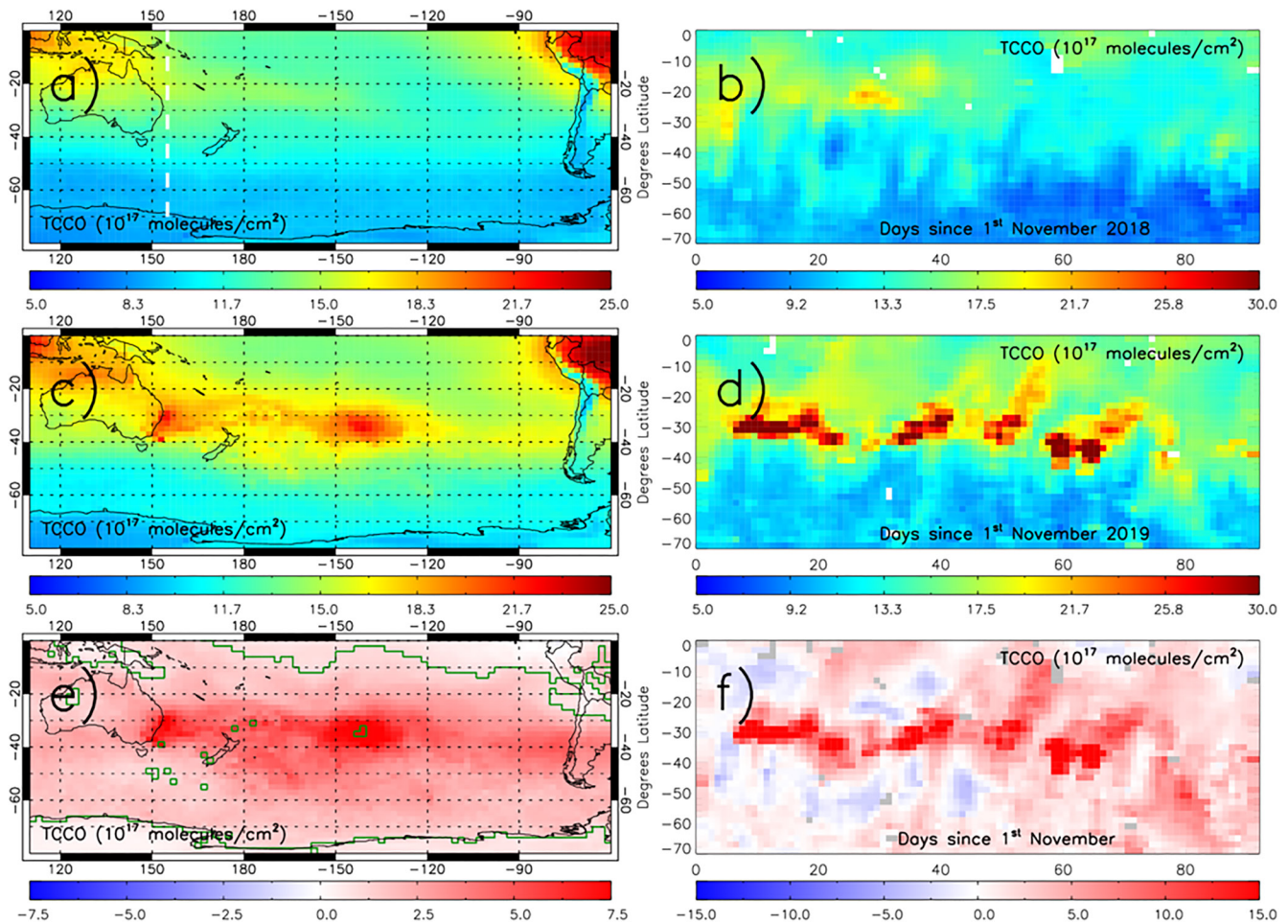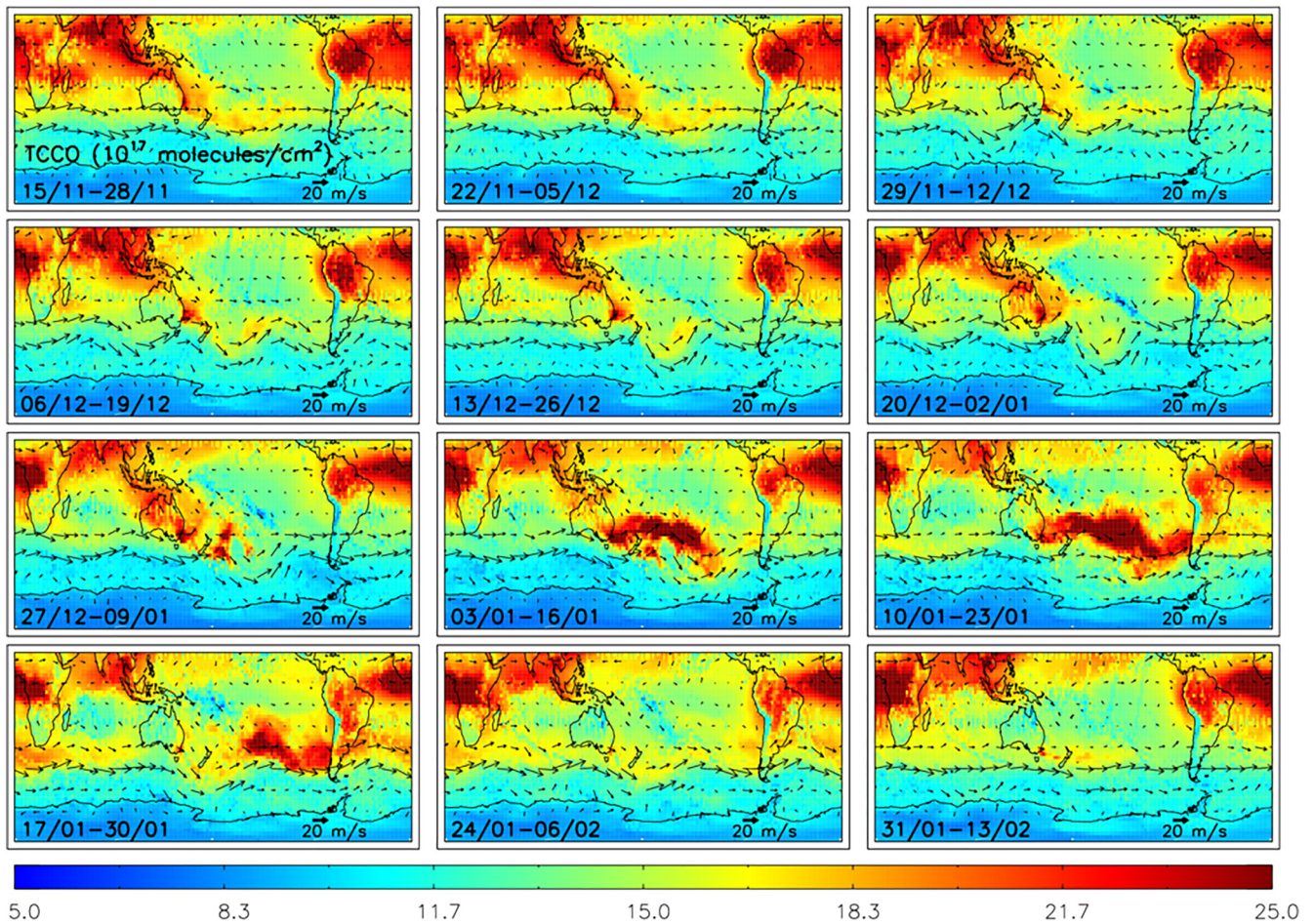
Figure 3. Infrared Atmospheric Sounding Interferometer (IASI) November-December-January (NDJ) total-column carbon monoxide (TCCO, 10^{17} molecules/cm^2) for (a) 2018/2019, (c) 2019/2020, and (e) 2019/2020–2018/2019 difference. Green polygon-outlined regions in panel (e) represent statistically significant differences between the fire seasons at the 99% confidence level (CL, based on the Student t-test) and where absolute differences are greater than 1.0×10^{17} molecules/cm^2. Panels (b), (d), and (f) represent Hovmöller diagrams of IASI TCCO from November to January at 155°E, between 70°S and 0°S (white dashed line in panel (a)), for 2018/2019, 2019/2020, and 2019/2020–2018/2019 difference, respectively.

We can also use IASI TCCO measurements to investigate the emission of CO from these fires. Figure 5 represents the daily CO burden for three regions, labeled Boxes 1–3 in Figure 5, and highlights step changes in the burden with time associated with fresh CO emission. For Box 1, there are two large step changes (Day 60 to Day 61 and Day 64 to Day 65) of approximately 4.0 and 7.0 Tg, respectively. A few days later as the plume enters Box 2, the step changes are approximately 8.0 Tg in both cases (i.e., Day 61 to Day 63 and Day 65 to Day 67). As the CO plume propagates eastwards, it is subject to chemical processing and entrainment of clean air, but as the plume rises, it likely enters an altitude of increased IASI vertical sensitively allowing for more CO to be detected. As the CO plume enters Box 3, the step changes are approximately 3.0 Tg (Day 62 to Day 65) and 4.0 Tg (Day 77 to Day 79). Therefore, between the December 30, 2019 and January 4, 2020, there were two large pulses of CO emission from the Australian fires, each in the order of approximately 6–8 Tg. Though it should be noted that this approach assumes limited chemical processing of the emitted CO as it propagates across the South Pacific and that there is limited meridional transport out of the boxes, especially Boxes 1 and 2.

3.4. Methanol and Methane

Focusing on January 3–16, 2020, when the fire plumes were most spatially extensive (see TCCO in Figures 4 and 6a), CH$_3$OH and CH$_4$ both showed substantial increases from the fires (Figures 6b and 6c). Total column

Figure 4. Temporal evolution of the Infrared Atmospheric Sounding Interferometer (IASI) mean total-column carbon monoxide (TCCO) (10^{17}molecules/cm^2) between the November 15, 2019 and February 13, 2020. Each panel represents a 2-week average with a weekly step between the first day of each map. The arrows show 500 hPa winds from the National Centers for Environmental Prediction reanalysis.

CH$_3$OH (TCCH$_3$OH), relative to January 3–16, 2019, show peak enhancements of over 15×10^{15} molecules/cm^2 co-locating with TCCO enhancements of over 15×10^{17} molecules/cm^2 (Figure 6a). Though CH$_3$OH infrared absorption features are much weaker than those of CO and low background CH$_3$OH abundances (e.g., over the ocean) are difficult to detect in individual soundings (i.e., large estimated errors; see Text S2, Figure S5), robust signals are detected in large sources such as the Australian fire plume (i.e., $>15 \times 10^{15}$ molecules/cm^2, Figure 6b, Text S2, Figure S6).

CH$_4$, on spatial and temporal scales observable by satellite fluctuates by only a few percent of its global mean value, unlike the order of magnitude of variability in CO and CH$_3$OH. To retrieve CH$_4$ perturbations at the percent level requires careful handling of cloud and, in the case of the Australian wildfire plumes, also smoke (and dust). As shown in Text S3 and Figure S9, IASI detects daily CO plumes, but the corresponding CH$_4$ distribution is less well sampled due to stringent filtering necessary for cloud. To detect the methane signal associated with Australian wildfires in this particular season in the presence of other sources of inter-year variability is at the percent level. However, the column average CH$_4$ (CACH$_4$) trend-adjusted anomaly for the January 3–16, 2020 was determined, with reference to the de-trended and de-seasonalized multiannual mean for January (2007–2017, MetOp-A & B offline version) (Figure 6c). This anomaly is positive at the >0.01 ppmv level over much of the region, and some features (e.g., 0.015–0.03 ppmv) cohere with prominent structure (e.g., over the central South Pacific) in the CO and CH$_3$OH plumes (see Figures 6a and 6b). Therefore, we use CO as an in-plume tracer to quantify the much lower amplitude CH$_4$ signals from the fires. In this case, the TCCO data is subject to the stricter cloud filtering as applied to TCCH$_4$ and
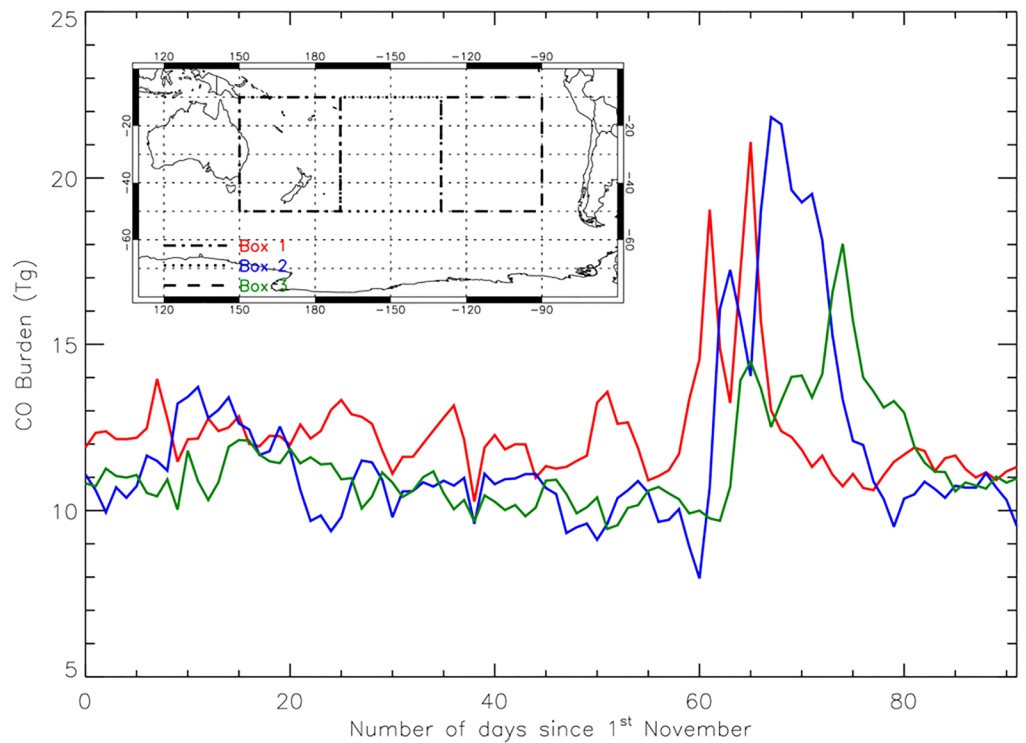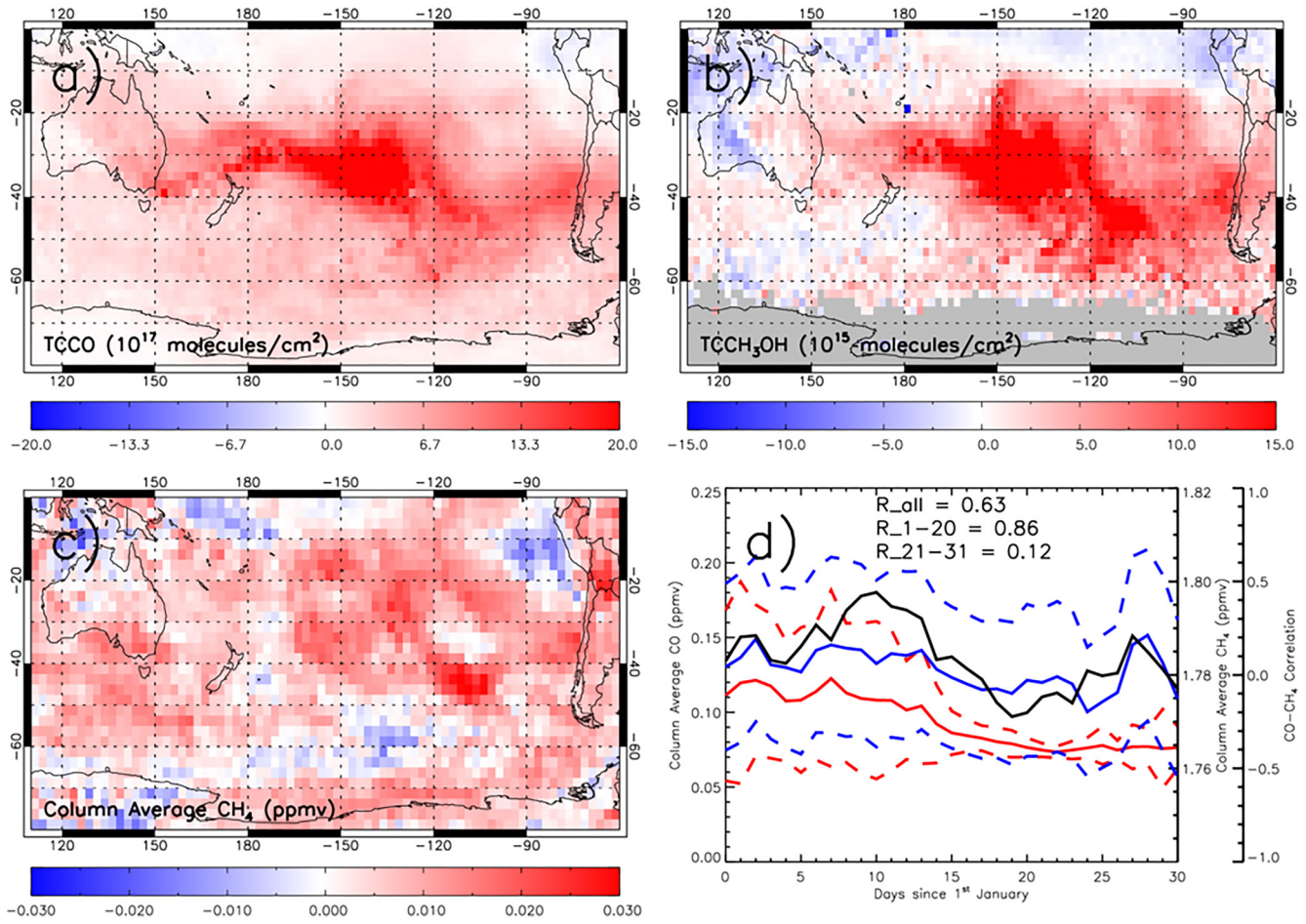
Figure 5. Daily Infrared Atmospheric Sounding Interferometer (IASI) derived CO burden (Tg) between the November 1, 2019 and January 31, 2020 for three regions: Box 1 (red line), Box 2 (blue line), and Box 3 (green line).

a given IASI sounding is used only when retrievals of both species are available, to reduce sampling errors. Figure 6d shows the time evolution of in-plume column average CO (CACO) and $CACH_4$ averaged over 150°E−90°W, 50–20°S (black box in Figure S9). The in-plume thresholds for CACO and $CACH_4$ were subjectively set at 0.07 ppmv and 1.75 ppmv. Investigation of the sensitivity of the $CACH_4$ (CACO) threshold between 1.73 (0.065) and 1.77 (0.075) ppmv highlights a limited impact on the results in Figure 6d. Both thresholds had to be met, along with stringent cloud screening and other quality control for CH_4, in order for the pair of CO and CH_4 soundings at a given location to be sampled.

In the first two weeks of January 2020, the in-plume domain-averaged daily CACO ranges between 0.09 and 0.12 ppmv, and the standard deviation indicates large spatial variability. In the second two weeks of January, the spatially averaged CACO is substantially lower, ranging between 0.07 and 0.08 ppmv, with much smaller spatial variability, consistent with mixing with neighboring CO-poor airmasses in the east and less intense incoming plumes in the west. In contrast, for $CACH_4$ the spatially averaged value drops only slightly and spatial variability is unchanged in the second two weeks, attributable to mixing with high CH_4 tropical airmasses in the east. The peak average $CACH_4$ values (1.78–1.79 ppmv) occur in the first few weeks and then January 27–29. Temporal correlation of the spatially averaged CO and CH_4 time series is 0.63 for the whole month and 0.86 between January 1 and 20. The daily spatial correlation in this period is between 0.2 and 0.5, indicative of a substantial fire-induced component of CH_4. Here, these $CO:CH_4$ correlations are based on the Pearson correlation coefficient and are significant at 95% confidence level or higher. In the latter period of January (21–31) the correlation drops below 0.0 indicating the fire-induced component to be less significant for CH_4 in comparison to other processes. Overall, the relationship between CO and CH_4 in data produced from IASI on MetOp-B demonstrates that the plumes emitted from the Australian fires contained CH_4 as well as CO. Emission factors of CH_4 from vegetation fires have been shown to be similar in magnitude to those of CH_3OH on a mass emitted per mass of dry matter consumed basis (Akagi et al., 2011). It is worth noting that given the long lifetime of CH_4 against hydroxyl radical (OH) oxidation (~9 years (McNorton et al., 2016)), any enhancement in CH_4 due to OH suppression in the plume on the transport timescale of a few days would be minimal (~0.1% over 3 days under complete suppression of OH oxidation).

Figure 6. (a) Infrared Atmospheric Sounding Interferometer (IASI) two-week (January 3–16) 2020–2019 difference total-column carbon monoxide (TCCO) (10^{17}molecules/cm^2) and (b) total column methanol (TCCH$_3$OH, 10^{15}molecules/cm^2). Gray regions represent missing satellite data (i.e., average values with error terms $>15.0 \times 10^{15}$ molecules/cm^2). (c) Two-week (January 3–16, 2020) column average methane (CH$_4$, ppmv) anomaly with respect to the de-seasonalized and de-trended multi-annual mean for January (2007–2017). (d) Daily time series of spatially averaged in-plume (150°E−90°W, 50–20°S; black box in Figure S9) IASI-observed CO (red) and CH$_4$ (blue) column average mixing ratios for January 2020. In-plume data are defined where CO and CH$_4$ values are both larger than the corresponding thresholds of 0.07 and 1.75 ppmv. Dashed lines represent the uncertainty range (average ± standard deviation). The black line represents daily spatial correlations between in-plume CO and CH$_4$. R_all, R_1–20 and R_21–31 are the CO-CH$_4$ time series correlations for all of January, January 1–20 and January 21–31, respectively.

3.5. Enhancement Ratios

We investigate how the TCCH$_3$OH:TCCO enhancement ratio changes as the fire plume traverses the Pacific across the four regional boxes defined in Figure 7a between the January 1 and 17 2020 (i.e., period of large fire plumes). Box 1 covers the primary fire region and Boxes 2–4 cover the downwind outflow. In all cases, we see TCCO-TCCH$_3$OH correlation values (R in Figures 7c–7f) above 0.63, peaking at 0.92 in Box 3, indicative of common origins. The in-plume TCCO and TCCH$_3$OH values are defined based on a subjectively chosen threshold (TCCO = 18.0×10^{17} molecules/cm^2 and TCCH$_3$OH = 5.0×10^{15} molecules/cm^2, where both criteria have to be met for the two species to be co-sampled), but sensitivity analysis of these thresholds (Text S4, Table S1), and the time period in which the plume(s) are sampled, show that our results are robust and relatively insensitive to our choices of these parameters.

In Box 1, the TCCH$_3$OH:TCCO enhancement ratio (M), based on a simple linear least-squares fit, is 0.0036 ± 5.98%, which is similar to the FINN CH$_3$OH:CO fire emissions ratio (0.0031 ± 0.04%). This suggests that the satellite observations of atmospheric enhancements close to the fires are consistent with freshly emitted fire pollution. As the plume propagates eastwards over the Pacific, there is an increase in the TCCH$_3$OH:TCCO enhancement ratio. In Boxes 2, 3, and 4 M is 0.0059 ± 3.13%, 0.0091 ± 1.28%, and
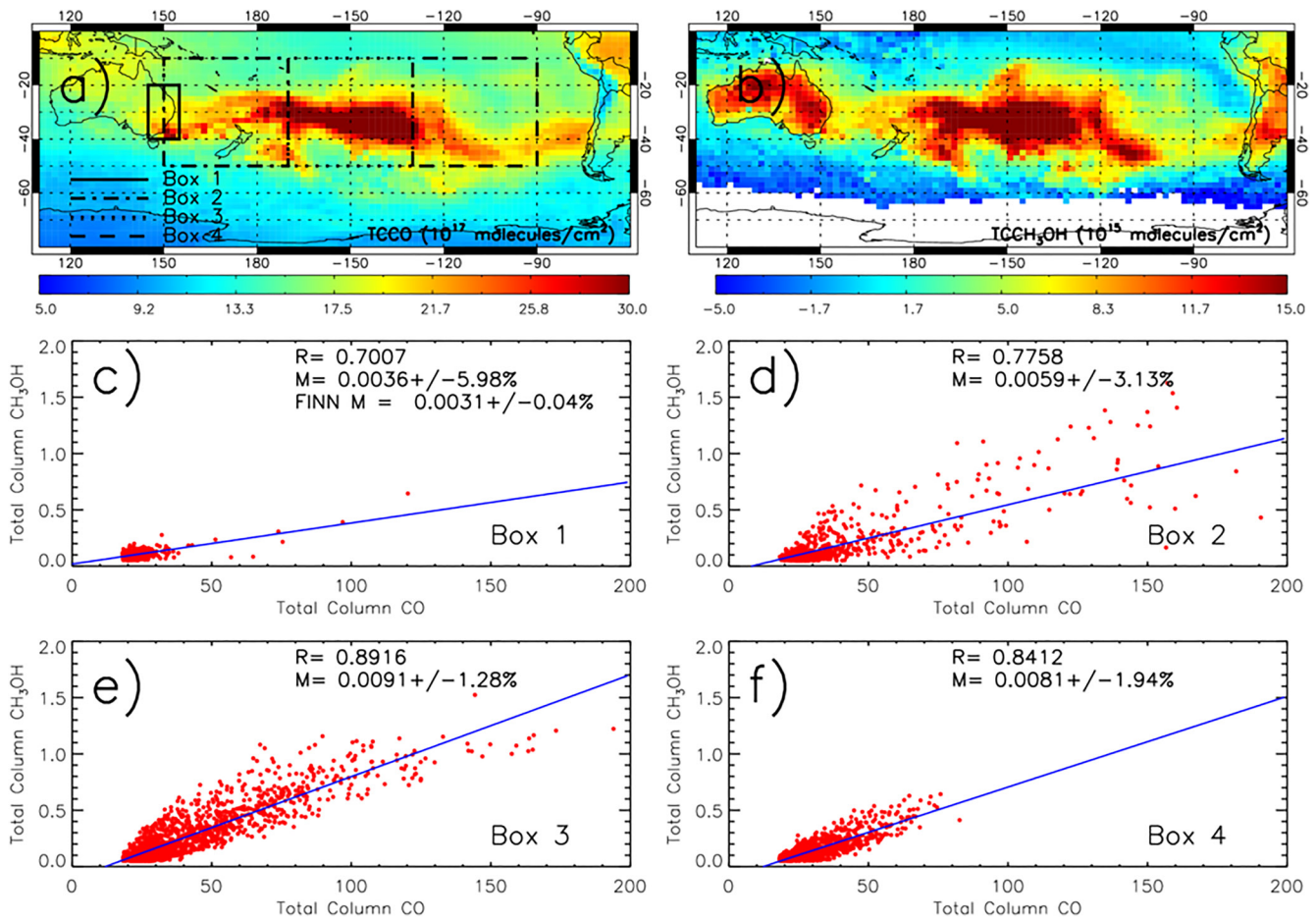
Figure 7. (a) total-column carbon monoxide (TCCO) and (b) total column methanol (TCCH$_3$OH) (10^{17} molecules/cm^2) for 1–17 January 2020. White regions represent missing satellite data (i.e., average values with error terms >15.0 × 10^{15} molecules/cm^2). Panels (c–f) show scatter plots of TCCH$_3$OH versus TCCO within Boxes 1–4 outlined in panel (a) with values of correlation (R) and gradient (enhancement ratio, M) indicated.

0.0081 ± 1.94%, respectively. When using the full range of the IASI TCCH$_3$OH retrievals (i.e., the retrieval values ± the random errors) and recalculating the enhancement ratios, we find that M is perturbed by approximately 10%, which is relatively small, and the regional ratios follow the same tendency. This increase of TCCH$_3$OH with distance, and therefore time, from the fires is suggestive of in-plume chemical production of CH$_3$OH. This is similar to Coheur et al. (2009) and Holzinger et al. (2005), who used aircraft and satellite data respectively, to investigate fire plume CH$_3$OH:CO enhancement ratios suggesting signs of secondary CH$_3$OH production when studying southern European fire plumes. The magnitude of the CH$_3$OH/CO enhancement ratios derived here are consistent with other studies (e.g., Christian et al., 2003; Holzinger et al., 2005; Karl et al., 2007; Singh et al., 2004; Yokelson et al., 1999). Our results imply that IASI detected such secondary formation of CH$_3$OH within the fire plume, but with a robust enhancement across the large portion of the Pacific, on a scale previously not discussed in the literature, to the best of our knowledge. Mixing with background air would likely dilute the plume counteracting some of the downwind increase in CH$_3$OH enhancement relative to CO. This suggests that the in-plume production of CH$_3$OH is likely larger than that suggested by the observed increase in the CH$_3$OH:CO ratio alone. Such large-scale enhancements in CH$_3$OH may have an important influence on the CH$_3$OH budget, impact the oxidative capacity of the remote atmosphere, and potentially the CH$_4$ lifetime (Read et al., 2012). Such secondary methanol production could be driven by the self-reaction of methylperoxy (CH$_3$O$_2$), the reaction of CH$_3$O$_2$ with higher order peroxy (RO$_2$) radicals (Jacob et al., 2005) and OH (Müller et al., 2016), or possibly by less well-established oxidation of organics in the fire plume (Holzinger et al., 2005).

4. Conclusions

The 2019/2020 Australian fires ("black summer") constituted some of the largest regional wildfires in recent decades and produced large quantities of smoke, aerosols, and trace gases. Peak fire activity occurred on eucalyptus forest vegetation in south-eastern Australia during December and January. Data from the MetOp-B satellite produced by RAL's NRT processing system show that carbon monoxide (CO) emitted from the fires circumnavigated the entire Southern Hemisphere (SH). Compared with the 2018/2019 fire season, to levels of CO from the fire plumes were substantially (and significantly, 99% confidence level) larger by approximately 30%–70% over the South Pacific in the November-December-January average.

Methanol (CH_3OH), which is difficult to detect in normal circumstances due to its weak absorption signature, was in sufficient abundance to retrieve in-plume column amounts with a good precision. Satellite-observed enhancements in total column CH_3OH relative to total column CO show a substantial increase downwind from the fires, over the Pacific Ocean. This is strongly suggestive of CH_3OH production within the plume, on a scale not previously reported, as far as we are aware, with potentially important implications for the methanol budget and oxidative capacity of the remote atmosphere. Elevated levels of CH_4 were also detected in association with the fire-plumes during peak activity in early to mid-January 2020, even though the CH_4 emission rate is considerably lower than for CO and perturbations from uniform mixing less than 2%. We also detected more localized enhancements in NO_2 in fire identified regions in South-Eastern Australia.

With future climate and land-use change it is expected that wildfires are going to become more frequent and intense. Therefore, Earth observation (EO), as presented here, is going to be a vital resource to help monitor and understand future wildfire events globally. These EO capabilities will improve with the planned launches of advanced infrared and shortwave spectrometers such as IASI Next Generation and Sentinel 5 on the MetOp Second Generation in polar orbit (ESA, 2020) and the Infrared Sounder and Sentinel 4 on Meteosat Third Generation in geostationary orbit.

Data Availability Statement

TROPOMI tropospheric column NO_2 data came from KNMI, which are available at https://www.temis.nl/airpollution/no2.php. FINN NRT vn1.5 burned area and GFAS FRP data came from NCAR (https://www.acom.ucar.edu/acresp/forecast/fire-emissions.shtml), and ECMWF-CAMS (https://apps.ecmwf.int/datasets/data/cams-gfas/). Meteorological reanalysis data waere obtained from NCEP (https://psl.noaa.gov/data/gridded/data.ncep.reanalysis.html). RAL's NRT system processes Eumetsat Level-1 data from MetOp-B IASI, MHS, AMSU, and GOME-2 and uses ECMWF meteorological forecast data, all processed on RAL's Jasmin infrastructure. We will upload the data to the UK Centre for Environmental Data Analysis (CEDA) archive upon acceptance. For the purposes of review, our data are available at http://homepages.see.leeds.ac.uk/~earrjpo/iasi_data/.

References

Akagi, S. K., Yokelson, R. J., Wiedinmyer, C., Alvarado, M. J., Reid, J. S., Karl, T., et al. (2011). Emission factors for open and domestic biomass burning for use in atmospheric models. *Atmospheric Chemistry and Physics*, *11*, 4039–4072. https://doi.org/10.5194/acp-11-4039-2011

Alvarado, M. J., Logan, J. A., Mao, J., Apel, E., Riemer, D., Blake, D., et al. (2010). Nitrogen oxides and PAN in plumes from boreal fires during ARCTAS-B and their impact on ozone: An integrated analysis of aircraft and satellite observations. *Atmospheric Chemistry and Physics*, *10*, 9739–9760. https://doi.org/10.5194/acp-10-9739-2010

Andela, N., Morton, D. C., Giglio, L., Chen, Y., van der Werf, G. R., Kasibhatla, P. S., et al. (2017). A human-driven decline in global burned area. *Science*, *356*, 1356–1362. https://doi.org/10.1126/science.aal4108

Australian Bureau of Meteorology. (2020). *Annual climate statement 2019*. Retrieved from http://www.bom.gov.au/climate/current/annual/aus

BBC. (2020). *Australia fires: A visual guide to the bushfire crisis*. Retrieved from https://www.bbc.co.uk/news/world-australia-50951043

Bowman, M. J. S., & Johnston, F. H. (2005). Wildfire smoke, fire management, and human health. *EcoHealth*, *2*, 76–80. https://doi.org/10.1007/s10393-004-0149-8

Bradstock, R. A., Cary, G. J., Davies, I., Lindenmayer, B. D., Price, O. F., & Williams, R. J. (2012). Wildfires, fuel treatment and risk mitigation in Australian eucalypt forests: Insights from landscape-scale simulation. *Journal of Environmental Management*, *105*, 66–75. https://doi.org/10.1016/j.jenvman.2012.03.050

Christian, T. J., Kleiss, B., Yokelson, R. J., Holzinger, R., Crutzen, P. J., Hao, W. M., et al. (2003). Comprehensive laboratory measurements of biomass-burning emissions: 1. Emissions from Indonesian, African, and other fuels. *Journal of Geophysical Research*, *108*, 4719. https://doi.org/10.1029/2003JD003704

Clarke, H. G., Smith, P. L., & Pitman, A. J. (2011). Regional signatures of future fire weather over eastern Australia from global climate models. *International Journal of Wildland Fire*, *20*(4), 550–562. https://doi.org/10.1071/WF10070

Clerbaux, C., Boynard, A., Clarisse, L., George, M., Hadji-Lazaro, J., Herbin, H., et al. (2009). Monitoring of atmospheric composition using the thermal infrared IASI/MetOp sounder. *Atmospheric Chemistry and Physics*, *9*, 6041–6054. https://doi.org/10.5194/acp-9-6041-2009

Coheur, P.-F., Clarisse, L., Turquety, S., Hurtmas, D., & Clerbaux, C. (2009). IASI measurements of reactive trace species in biomass burning plumes. *Atmospheric Chemistry and Physics*, *9*, 5655–5667. https://doi.org/10.5194/acp-9-5655-2009

Di Virgilio, G., Evans, J. P., Blake, S. A. P., Armstrong, M., Dowdy, A. J., Sharples, J., & McRae, R. (2019). Climate change increases the potential for extreme wildfires. *Geophysical Research Letters*, *46*, 8517–8526. https://doi.org/10.1029/2019gl083699

ESA. (2020). *Sentinel overview*. Retrieved from https://sentinel.esa.int/web/sentinel/missions

Giglio, L., Randerson, J. T., & van der Werf, G. R. (2013). Analysis of daily, monthly, and annual burned area using the fourth-generation global fire emissions dataset (GFED4). *Journal of Geophysical Research: Biogeosciences*, *118*, 317–328. https://doi.org/10.1002/jgrg.20042

Haikerwal, A., Akram, M., Sim, M. R., Meyer, M., Abramson, M. J., & Dennekamp, M. (2016). Fine particulate matter ($PM_{2.5}$) exposure during a prolonged wildfire period and emergency department visits for asthma. *Respirology*, *21*, 88–94. https://doi.org/10.1111/resp.12613

Holzinger, R., Williams, J., Salisbury, G., Klüpfel, T., de Reus, M., Traub, M., et al. (2005). Oxygenated compounds in aged biomass burning plumes over the East Mediterranean: Evidence of strong secondary production of methanol and acetone. *Atmospheric Chemistry and Physics*, *5*, 39–46. https://doi.org/10.5194/acpd-4-6321-2004

Hope, M. (2020). Australian burning. *The Lancet Planetary Health*, *4*(1), E12–E13. https://doi.org/10.1016/s2542-5196(20)30006-1

Illingworth, S. M., Remedios, J. J., Boesch, H., Moore, D. P., Sembhi, H., Dudhia, A., & Walker, J. C. (2011). ULIRS, an optimal estimation retrieval scheme for carbon monoxide using IASI spectral radiances: Sensitivity analysis, error budget and simulations. *Atmospheric Measurement Techniques*, *4*, 269–288. https://doi.org/10.5194/amt-4-269-2011

Jacob, D. J., Field, B. D., Li, Q., Blake, D. R., de Gouw, J., Warneke, C., et al. (2005). Global budget of methanol: Constraints from atmospheric observations. *Journal of Geophysical Research*, *110*, D08303. https://doi.org/10.1029/2004JD005172

Kablick, G. P., III, Allen, D. R., Fromm, M. D., & Nedoluha, G. E. (2020). Australian PyroCb smoke generates synoptic-scale stratospheric anticyclones. *Geophysical Research Letters*, *47*(13), e2020GL088101. https://doi.org/10.1029/2020GL088101

Kaiser, J. W., Hell, A., Andreae, M. O., Benedetti, A., Chubarova, N., Jones, L., et al. (2012). Biomass burning emissions estimated with a global fire assimilation system based on observed fire radiative power. *Biogeosciences*, *9*, 527–554. https://doi.org/10.5194/bg-9-527-2012

Karl, T. G., Christian, T. J., Yokelson, R. J., Artaxo, P., Hao, W. M., & Guenther, A. (2007). The tropical forest and fire emissions experiment: Method evaluation of volatile organic compound emissions measured by PTR- MS, FTIR, and GC from tropical biomass burning. *Atmospheric Chemistry and Physics*, *7*(22), 5883–5897. https://doi.org/10.5194/acp-7-5883-2007

Khaykin, S., Legras, B., Bucci, S., Sellitto, P., Isaksen, L., Tence, F., et al. (2020). The 2019/2020 Australian wildfires generated a persistent smoke-charged vortex rising up to 35 km altitude. *Communications Earth & Environment*, *1*, 22. https://doi.org/10.1038/s43247-020-00022-5

Kiely, L., Spracklen, D. V., WiedinmyerConibear, C. L., Reddington, C. L., Archer-Nicholls, S., Archer-Nicholls, S., et al. (2019). New estimate of particulate emissions from Indonesian peat fires in 2015. *Atmospheric Chemistry and Physics*, *19*, 11105–11121. https://doi.org/10.5194/acp-19-11105-2019

Li, F., Lawrence, D. M., & Bond-Lamberty, B. (2017). Impact of global land surface air temperature and energy budget for the 20th Century due to changes within ecosystems. *Environmental Research Letters*, *12*, 044014. https://doi.org/10.1088/1748-9326/aa6685

Logan, J. A. (1983). Nitrogen oxides in the troposphere: Global and regional budgets. *Journal of Geophysical Research*, *88*, 10785–10807. https://doi.org/10.1029/JC088iC15p10785

McNorton, J., Chipperfield, M. P., Gloor, M., Wilson, C., Feng, W., Hayman, G. D., et al. (2016). Role of OH variability in the stalling of the global atmospheric CH_4 growth rate from 1999 to 2006. *Atmospheric Chemistry and Physics*, *16*, 7943–7956. https://doi.org/10.5194/acp16-7943-201610.5194/acp-16-7943-2016

Müller, J.-F., Liu, Z., Nguyen, V. S., Stavrakou, T., Harvey, J. N., & Peeters, J. (2016). The reaction of methyl peroxy and hydroxyl radicals as a major source of atmospheric methanol. *Nature Communications*, *7*, 13213. https://doi.org/10.1038/ncomms13213

NPI. (2020). *National pollutant inventory*. Retrieved from http://www.npi.gov.au/npidata/action/load/browse-search/criteria/browse-type/Location/year/2019

Ohneiser, K., Ansmann, A., Baars, H., Seifert, P., Barja, B., Jimenez, C., et al. (2020). Smoke of extreme Australian bushfires observed in the stratosphere over Punta Arenas, Chile, in January 2020: Optical thickness, lidar ratios, and depolarization ratios at 355 and 532 nm. *Atmospheric Chemistry and Physics*, *20*, 8003–8015. https://doi.org/10.5194/acp-20-8003-2020

Pitman, A. J., Narisma, G. T., & McAneney, J. (2007). The impact of climate change on the risk of forest and grassland fires in Australia. *Climatic Change*, *84*, 383–401. https://doi.org/10.1007/s10584-007-9243-6

Rabin, S. S., Magi, B. I., Shevliakova, E., & Pacala, S. W. (2015). Quantifying regional, time-varying effects of cropland and pasture on vegetation fire. *Biogeosciences*, *12*, 6591–6604. https://doi.org/10.5194/bg-12-6591-2015

RAL Space (2015). *Optimal estimation method retrievals with IASI, AMSU and MHS – final Report Version 5.2*. Retrieved from http://ceda-docs.ceda.ac.uk/1377/1/iasi_mhs_final_report_v5p2.pdf

Read, K. A., Carpenter, L. J., Arnold, S. R., Beale, R., Nightingale, P. D., Hopkins, J. R., et al. (2012). Multiannual observations of acetone, methanol, acetaldehyde in remote tropical Atlantic air: Implications for atmospheric OVOC budgets and oxidative capacity. *Environmental Science Technology*, *46*(20), 11028–11039. https://doi.org/10.1021/es302082p

Reisen, F., Meyer, C. P., McCaw, L., Powell, J. C., Tolhurst, K., Keywood, M. D., & Gras, J. L. (2005). Impact of smoke from biomass burning on air quality in rural communities in southern Australia. *Atmospheric Environment*, *45*(24), 3944–3953. https://doi.org/10.1016/j.atmosenv.2011.04.060

Rowlinson, M. J., Rap, A., Arnold, S. R., Pope, R. J., Chipperfield, M. P., McNorton, J., et al. (2019). Impact of El Niño–southern oscillation on the interannual variability of methane and tropospheric ozone. *Atmospheric Chemistry and Physics*, *19*, 8669–8686. https://doi.org/10.5194/acp-19-8669-2019

Schwartz, M. J., Santee, M. L., Pumphrey, H. C., Manney, G. L., Lambert, A., Livesey, N. J., et al. (2020). Australian new year's PyroCb impact on stratospheric composition. *Geophysical Research Letters*, *10*(24), e2020GL090831. https://doi.org/10.1029/2020GL090831

Siddans, R., Knappett, D., Kerridge, B., Latter, B., & Waterfall, A. (2020). *STFC RAL methane retrievals from IASI on board MetOp-A, version 2.0*. Centre for Environmental Data Analysis. https://doi.org/10.5285/f717a8ea622f495397f4e76f777349d1

Siddans, R., Knappett, D., Kerridge, B. J., Waterfall, A., Hurley, J., Latter, B., et al. (2017). Global height-resolved methane retrievals from the infrared atmospheric sounding interferometer (IASI) on MetOp. *Atmospheric Measurement Techniques*, *10*, 4135–4164. https://doi.org/10.5194/amt-10-4135-2017

Siddaway, J. M., & Petelina, S. V. (2011). Transport and evolution of the 2009 Australian black saturday bushfire smoke in the lower stratosphere observed by OSIRIS on Odin. *Journal of Geophysical Research*, *116*, D06203. https://doi.org/10.1029/2010JD015162

Singh, H. B., Salas, L. J., Chatfield, R. B., Czech, E., Fried, A., Walega, J., et al. (2004). Analysis of the atmospheric distribution, sources, and sinks of oxygenated volatile organic chemicals based on measurements over the Pacific during TRACE-P. *Journal of Geophysical Research*, *109*, D15307. https://doi.org/10.1029/2003JD003883

SOTE. (2016). *Vegetation land*. Retrieved from https://soe.environment.gov.au/theme/land/topic/2016/vegetation-0

UoS. (2020). *More than one billion animals killed in Australian bushfires*. Retrieved from https://www.sydney.edu.au/news-opinion/news/2020/01/08/australian-bushfires-more-than-one-billion-animals-impacted.html

van der Werf, G. R., Randerson, J. T., Giglio, L., Collatz, G. J., Kasibhatla, P. S., Morton, D. C., et al. (2010). Global fires emissions and the contributions from deforestation, savannah, forest, agricultural and peat fires (1997-2009). *Atmospheric Chemistry and Physics*, *10*, 11707–11735. https://doi.org/10.5194/acp-10-11707-2010

van der Werf, G. R., Randerson, J. T., Giglio, L., van Leeuwen, T. T., Chen, Y., Rogers, B. M., et al. (2017). Global fire emission estimates during 1997-2016. *Earth System Science Data*, *9*, 697–720. https://doi.org/10.5194/essd-9-697-2017

Veefkind, J. P., Aben, I., McMullan, K., Forster, H., de Vries, J., Otter, G., et al. (2012). TROPOMI on the ESA Sentinel-5 Precursor: A GMES mission for global observations of the atmospheric composition for climate, air quality and ozone layer applications. *Remote Sensing of Environment*, *120*, 70–83. https://doi.org/10.1016/j.rse.2011.09.027

Wiedinmyer, C., Akagi, S. K., Yokelson, R. J., Emmons, L. K., Al-Saadi, A. J., Orlando, J. J., & Soja, A. J. (2011). The Fire INventory from NCAR (FINN): A high resolution global model to estimate the emissions from open burning. *Geoscientific Model Development*, *4*, 624–641. https://doi.org/10.5194/gmd-4-625-2011

Wooster, M. J., Gaveau, D. L. A., Salim, M. A., Zhang, T., Xu, W., Green, D. C., et al. (2018). New tropical peatland gas and particulate emissions factors indicate 2015 Indonesian fires release far more particulate matter (but Less Methane) than current inventories imply. *Remote Sensing*, *10*(4), 495. https://doi.org/10.3390/rs10040495

Yokelson, R. J., Goode, J. G., Ward, D. E., Susott, R. A., Babbitt, R. E., Wade, D. D., et al. (1999). Emissions of formaldehyde, acetic acid, methanol, and other trace gases from biomass fires in North Carolina measured by airborne Fourier transform infrared spectroscopy. *Journal of Geophysical Research*, *104*, 30109–30125. https://doi.org/10.1029/1999jd900817

References From the Supporting Information

Apel, E. C., Emmons, L. K., Karl, T., Hills, A. J., Madronich, S., Lee-Taylor, J., et al. (2010). Chemical evolution of volatile organic compounds in the outflow of the Mexico City metropolitan area. *Atmospheric Chemistry and Physics*, *10*, 2353–2375. https://doi.org/10.5194/acp-10-2353-2010

Apel, E. C., Hornbrook, R. S., Hills, A. J., Blake, N. J., Barth, M. C., Weinheimer, A., et al. (2015). Upper tropospheric ozone production from lightning NO_x-impacted convection: Smoke ingestion case study from the DC3 campaign. *Journal of Geophysical Research: Atmospheres*, *120*, 2505–2523. https://doi.org/10.1002/2014JD022121

Bates, K. H., Jacob, D. J., Wang, S., Hornbrook, R. S., Apel, E. C., Kim, M. J., et al. (2021). The global budget of atmospheric methanol: New constraints on secondary, oceanic, and terrestrial sources. *Journal of Geophysical Research: Atmospheres*, *126*, e2020JD033439. https://doi.org/10.1029/2020JD033439

CAMS (2020). *Validation report for the CAMS global reanalysis of aerosols and reactive gases, years 2003-2019*. Retrieved from https://atmosphere.copernicus.eu/sites/default/files/2020-04/CAMS84_2018SC2_D5.1.1-2019.pdf

Franco, B., Clarisse, L., Stavrakou, T., Muller, J.–F., Van Damme, M., Whitburn, S., et al. (2018). A general framework for global retrievals of trace gases from IASI: Application to methanol, formic acid and PAN. *Journal of Geophysical Research*, *123*, 13963–13984. https://doi.org/10:1029/2018JD029633

Razavi, A., Karagulian, F., Clarisse, L., Hurtmans, D., Coheur, P. F., Clerbaux, C., et al. (2011). Global distributions of methanol and formic acid retrieved for the first time from the IASI/MetOp thermal infrared sounder. *Atmospheric Chemistry and Physics*, *11*, 857–872. https://doi.org/10.5194/acp-11-857-2011

Rodgers, C. D. (2000). *Inverse methods for atmospheric sounding: Theory and practice*. New Jersey, USA: World Science.

Siddans, R., Gerber, D., & Bell, B. (2015). *Optimal estimation method retrievals with IASI, AMSU and MHS measurements*. Final Report, EUM/CO/13/46000001252/THH.

Siddans, R., Walker, J., Latter, B., Kerridge, B., Gerber, D., & Knappett, D. (2018). *RAL Infrared Microwave Sounder (IMS) temperature, water vapour, ozone and surface spectral emissivity*. Centre for Environmental Data Analysis. https://doi.org/10.5285/489e9b2a0abd43a491d5afdd0d97c1a4

Wang, Y., Yong-Feng, M., Eskes, H., Inness, A., Flemming, J., & Brasseur, G. P. (2020). Evaluation of the CAMS global atmospheric trace gas reanalysis 2003–2016 using aircraft campaign observations. *Atmospheric Chemistry and Physics*, *20*, 4493–4521. https://doi.org/10.5194/acp-20-4493-2020

Wofsy, S. C., Afshar, S., Allen, H. M., Apel, E. C., Asher, E. C., Barletta, B., et al. (2018). *ATom: Merged atmospheric chemistry, trace gases, and aerosols*. Oak Ridge, TN: ORNL DAAC. https://doi.org/10.3334/ORNLDAAC/1581